energies

MDPI

Article

The Thermal Balance Temperature Field of the Electro-Hydraulic Servo Pump Control System

Guishan Yan [1,2], Zhenlin Jin [1,2,*], Mingkun Yang [1] and Bing Yao [1]

[1] School of Mechanical Engineering, Yanshan University, Qinhuangdao 066004, China; gsyan@stumail.ysu.edu.cn (G.Y.); ymk0915@stumail.ysu.edu.cn (M.Y.); yaobing@stumail.ysu.edu.cn (B.Y.)
[2] Heavy-Duty Intelligent Manufacturing Equipment Innovation Center of Hebei Province, Qinhuangdao 066004, China
* Correspondence: zljin@ysu.edu.cn; Tel.: +86-0335-8074783

Abstract: The electro-hydraulic servo pump control system (EHSPCS) is a high-performance control unit that integrates a permanent magnet synchronous motor (PMSM) and a closed hydraulic system (CHS). The design features of high integration and a high power-weight ratio lead to the poor heat dissipation capacity and high thermal balance temperature of the system. Excessive temperature will seriously affect the system's performance and service life. Therefore, the thermal balance analysis method of the EHSPCS under different loads and different wind speeds was proposed in this paper. Firstly, the PMSM and CHS were taken as research objects to analyze the heating source of the system. The thermal power model was established, and the calculation was performed. The variation rule of the thermal power generated by each component with the load torque under the typical rotating speed was obtained. Secondly, the system's temperature field thermal balance solution model was established. ANSYS and AMESim software were used to calculate the thermal balance points of the PMSM and CHS under different working conditions. The change rule of the thermal balance temperature field of the EHSPCS under different loads was analyzed with the conditions of the natural cooling and forced wind cooling of the PMSM. Finally, an experimental platform was built for experimental research, and the experimental temperature of the system under different loads and different wind speeds was measured. Through comparison and analysis with the simulation results, the correctness and feasibility of the thermal balance theoretical analysis method were verified. The research results will lay the foundation for thermal balance research on the EHSPCS, and have guiding significance for system design, component selection, and load matching.

Keywords: electro-hydraulic servo pump control system (EHSPCS); permanent magnet synchronous motor (PMSM); closed hydraulic system (CHS); thermal balance; temperature field

check for updates

Citation: Yan, G.; Jin, Z.; Yang, M.; Yao, B. The Thermal Balance Temperature Field of the Electro-Hydraulic Servo Pump Control System. *Energies* **2021**, *14*, 1364. https://doi.org/10.3390/en14051364

Academic Editor: Pablo Olmeda

Received: 27 January 2021
Accepted: 25 February 2021
Published: 2 March 2021

Publisher's Note: MDPI stays neutral with regard to jurisdictional claims in published maps and institutional affiliations.

Copyright: © 2021 by the authors. Licensee MDPI, Basel, Switzerland. This article is an open access article distributed under the terms and conditions of the Creative Commons Attribution (CC BY) license (https://creativecommons.org/licenses/by/4.0/).

1. Introduction

Electro-hydraulic servo pump control technology plays a very important role in high-precision control fields, e.g., aircraft rudder surface control [1], robot joint drives [2], and wind power variable paddle control [3], and is a core technology in industrial development. The electro-hydraulic servo pump control system (EHSPCS) adopts the concept of volumetric speed regulation under the permanent magnet synchronous motor (PMSM) drive mechanism. By changing the output speed and torque of the PMSM, the output flow and pressure of the fixed displacement pump can be controlled to achieve high-precision control of the position and force of the hydraulic cylinder. The introduction of electro-hydraulic servo pump control technology reduces the installation, operation, and maintenance costs of the system, improves the power-weight ratio and reliability [4–6], and solves the inherent defects of traditional valve control technology, namely, a high throttling loss, a high maintenance cost, and low integration [7], but the highly integrated design characteristics of the EHSPCS greatly reduce the effective heat dissipation area. Part of the heat converted by the electrical conductivity loss of the motor, the leakage loss of the fixed displacement

pump and the hydraulic cylinder is dissipated into the surrounding environment through the shell, and the other part is trapped inside the component, causing the temperature of the system to rise [8,9]. When the PMSM temperature is too high, a high temperature alarm and shutdown will often occur. If the hydraulic oil temperature is too high, it will cause the oil to oxidize and decrease its viscosity, increase system leakage, and increase component wear. To ensure that the system can run stably for a long time, the research on the thermal balance temperature field of the EHSPCS becomes crucial.

In recent years, relevant experts and scholars have continued their research on the heating problem of the PMSM and the closed hydraulic system (CHS) in the EHSPCS. Currently, calculation methods of the motor thermal field include the Lumped Parameter Thermal Network Method (LPTN), the Finite Element Method (FEM), and Computational Fluid Dynamics (CFD) [10]. In [11,12], an LPTN model for thermal design and analysis of the PMSM was presented, and the model predicted the temperature of each part of the motor with high precision. References [13,14] presented an electromagnetic-thermal coupling analysis method of the PMSM, which was based on current harmonics and improved the $(\mu + 1)$ evolution strategy. In [15], the thermal issues of a high-speed permanent-magnet motor were studied based on CFD and numerical heat-transfer calculations, and the reasons for the overheat of the prototype in the experimental test were thoroughly analyzed. In [16], a PMSM comprehensive CFD model was presented, and the comparison between measured and simulated temperatures showed that the model sufficiently described the thermal behavior of the motor. The thermal modeling analysis of the CHS mainly includes modeling software and the lumped parameter method. In [17], the characteristics of thermal generation and the dissipation of hydraulic components were analyzed, and the AMESim thermal model of the whole hydraulic system was established. In [18], a thermal-hydraulic model of a piston pump was constructed in AMESim. In [19], a set of lumped parameter mathematical models was developed. These models were based on the conservation of mass and energy, and the connection rule and method of the thermal-hydraulic components were proposed. In [20], a novel thermal-hydraulic pump model by the lumped parameter method was proposed, and a precise model of leakage flow and dynamic viscosity was introduced into it. Aiming at the thermodynamic research of EHSPCS, in [21,22], a lumped-parameter thermal-hydraulic model of the hydraulic part in the EHSPCS was proposed, and both the steady state and the transient temperature behavior of the system were quickly and accurately given by the model.

To solve the problems of the poor heat dissipation capacity and the high overload temperature in the EHSPCS, the heat source of the system was analyzed. A thermal power model of the PMSM and CHS under different working conditions was established. Maxwell and Matlab software were used to solve and calculate the thermal power of the PMSM and CHS under typical rotation speeds and different loads. The thermal balance solution model of the motor temperature field was established, and the temperature field of the motor under different loads was obtained with the conditions of natural cooling and forced wind cooling through ANSYS software. AMESim software was used to establish the simulation model of the CHS, and the temperature parameters of the thermal balance point of each part of the system under different working conditions were obtained. Finally, the thermal balance action law of the system was obtained. The experimental platform was built to conduct experimental research on the temperature field of the PMSM under the conditions of natural cooling and forced wind cooling, and the thermal balance temperature of the system under different loads and different wind speeds was obtained. Through the comparison of experimental data and theoretical analysis, the correctness and feasibility of the solution method for the temperature field of the EHSPCS were verified.

2. Working Principle of the EHSPCS

In the EHSPCS, the PMSM coaxial drives the fixed displacement pump, the suction and discharge ports of the fixed displacement pump are directly connected to the two load ports of the hydraulic cylinder, and the controller outputs control instructions to the PMSM

to change the rotation speed and torque of the fixed displacement pump, so as to adjust the displacement and force of the hydraulic cylinder. The accumulator and check valve are used to replenish oil in the oil filling circuit. The safety circuit uses the pressure relief valve to prevent the pressure of the two chambers of the hydraulic cylinder from being too high. The hydraulic circuit of the system is shown in Figure 1.

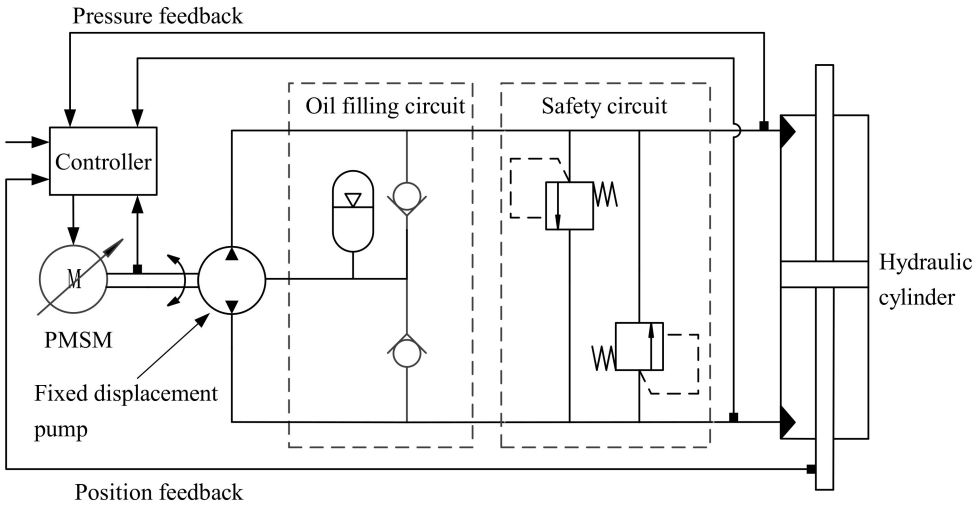

Figure 1. Hydraulic circuit of the electro-hydraulic servo pump control system (EHSPCS).

In this study, this system is a position control system. The system collects the difference between the actual position and the given position of the hydraulic cylinder through the displacement sensor, controls the PMSM speed through the control algorithm, and then controls the output flow of the fixed displacement pump to control the position change of the hydraulic cylinder, so as to realize the normal operation of the system. The fixed displacement pump in this study uses a radial piston pump.

3. Thermal Power Analysis

The thermal power loss of the EHSPCS can be divided into PMSM thermal power loss and CHS thermal power loss. The thermal power loss of the CHS can be further divided into the thermal power loss of the hydraulic pump, auxiliary parts, and hydraulic cylinder. In this study, a thermal power loss calculation model was established for the heating source of the system, and the thermal power of the heating source was solved and analyzed.

3.1. Establishment of PMSM Thermal Power Model

The loss in the working process of the motor is the main source of motor heating. Motor losses are mainly divided into stator iron loss, winding copper loss, and mechanical loss [23–27], the motor loss can be expressed as:

$$P_{\mathrm{m}} = P_{\mathrm{Fe}} + P_{\mathrm{Cu}} + P_{\mathrm{me}} \tag{1}$$

where P_{m} is the total motor loss (W), P_{Fe} is the stator iron loss (W), P_{Cu} is the winding copper loss (W), and P_{me} is the mechanical loss (W).

3.2. Solution of PMSM Thermal Power

PMSM power loss was calculated based on ANSYS software. PMSM basic parameters are shown in Table 1.

Table 1. Permanent magnet synchronous motor (PMSM) basic parameters.

Parameters	Value
Rated voltage (V)	380
Rated power (W)	7367
Rated speed (r/min)	2500
Copper wire resistivity (kg/m^3)	1.75×10^{-8}
Number of series turns per phase winding	72
Copper wire diameter (m)	1.12×10^{-3}
Rotor radius (m)	3.45×10^{-2}
Rotor axial length (m)	0.34

Since the electromagnetic performance of each part in the PMSM is symmetrical about the axial center plane, it is only necessary to establish a 1/2 model about the axial center plane when solving the electromagnetic field. The PMSM analytical model is shown in Figure 2.

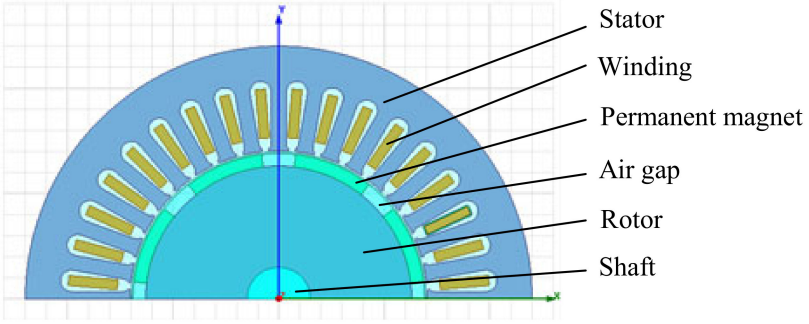

Figure 2. PMSM analytical model.

Based on the PMSM thermal power analytical model, the thermal power loss of the stator iron loss, winding copper loss, and mechanical loss at a typical rotating speed of the PMSM (500 r/min) is shown in Table 2 and Figure 3.

Table 2. PMSM part losses under different torques.

Torque	Iron Loss	Copper Loss	Mechanical Loss	Total Loss
(Nm)	(W)	(W)	(W)	(W)
0	12.51	0	0.5	13.01
10	20.22	60.5	0.5	81.22
20	32.23	137.91	0.5	170.64
28	38.58	220.43	0.5	259.51

It can be seen in Table 2 and Figure 3 that the copper loss and iron loss are the main heat sources, and the mechanical loss accounts for the smallest proportion. From the perspective of the proportion, iron loss is the main heat source of PMSM under low torque, and the copper loss gradually becomes the main heat source of PMSM as the torque increases.

3.3. Establishment of the CHS Thermal Power Model

The CHS includes a radial piston pump, a hydraulic cylinder, hydraulic pipelines, valve blocks, hydraulic valves, etc. The thermal power analysis of these components is the basis for studying the thermal balance characteristics of the system.

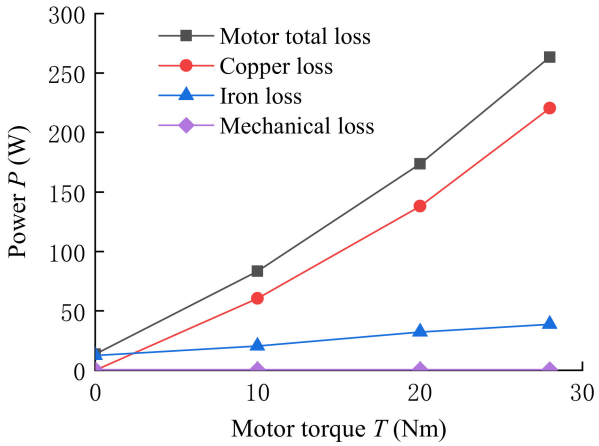

Figure 3. PMSM part losses under different torques.

3.3.1. Thermal Power Model of the Radial Piston Pump

The losses of radial piston pumps include volume loss and mechanical loss, volume loss refers to the heat generated by the oil leaking into the shell through the three major leakage pairs (piston pair, sliding shoe pair, and distribution pair) during the operation of the piston pump, and mechanical loss refers to the heat generated by the friction between oil and rotor, shaft and bearing with the rotation of the radial piston pump [28]. Compared with volume loss, mechanical loss is negligible at low speed.

In the working process of the piston pump, under the action of centrifugal force, the piston and the cylinder bore generate eccentric clearance. The differential pressure of the pump causes the differential pressure flow in the clearance. The leakage between a single piston and the cylinder bore can be expressed as:

$$Q_{L1} = \frac{\pi d_p \delta_p^3 \Delta p}{12 \mu L_P} \left(1 + 1.5\varepsilon^2\right) \tag{2}$$

where Q_{L1} is the leakage between a single piston and the cylinder bore (m^3/s), d_p is the piston diameter (m), δ_p is the clearance between the piston and the inner wall of the rotor piston bore (m), Δp is the differential pressure of suction and discharge ports of the radial piston pump (Pa), μ is the oil dynamic viscosity (Pa·s), L_p is the contact length between the piston and the cylinder bore, and ε is the eccentricity ratio.

The leakage of sliding shoe pair of radial piston pump is the result of oil fluid flowing around through the clearance between the sliding shoe and the stator. The pressure of the oil cavity in the center of the sliding shoe and the pressure of the shell cause the clearance to produce differential pressure flow. The leakage between a single sliding shoe and the swash plate can be expressed as:

$$Q_{L2} = \frac{\pi h^3 \Delta p}{6 \mu ln \frac{r_2}{r_1}} \tag{3}$$

where Q_{L2} is the leakage between a single sliding shoe and the swash plate (m^3/s), h is the thickness of the oil film between the stator and the sliding shoe (m), r_1 is the inner radius of the slipper seal oil belt (m), and r_2 is the outer radius of the slipper seal oil belt (m).

The leakage caused by the matching clearance between the flow distribution shaft and the rotor is usually simplified as the parallel surface clearance flow. The leakage between the flow distribution shaft and the rotor can be expressed as:

$$Q_{L3} = \frac{\varphi_v r_v \delta_v^3}{12 u L_v} \Delta p \tag{4}$$

where Q_{L3} is the leakage between the flow distribution shaft and the rotor (m^3/s), φ_v is the leak angle (rad), r_v is the flow distribution shaft radius (m), δ_v is the clearance between the piston and the rotor (m), and L_v is the contact length (m).

According to the above analysis, the total heat generation power of the radial piston pump can be given by:

$$P_p = \left[\sum_{i=1}^{N}(Q_{L1} + Q_{L2}) + Q_{L3}\right]\Delta p \tag{5}$$

where P_p is the total heat generation power of the radial piston pump (W). N is the number of pistons of the radial piston pump.

3.3.2. Thermal Power Model of the Hydraulic Cylinder

The internal leakage caused by the clearance between the piston of the hydraulic cylinder and the inner wall of the cylinder can be regarded as an annular clearance flow, and the heat generation power of the hydraulic cylinder is can be expressed as:

$$P_{cy} = \frac{\pi d_{cy}\delta_{cy}^3\left(p_{cyh} - p_{cyl}\right)}{12\mu l_{cy}} \tag{6}$$

where P_{cy} is the thermal power loss of hydraulic cylinder (W), p_{cyh} is the high pressure chamber pressure of the hydraulic cylinder (Pa), p_{cyl} is the low pressure chamber pressure of the hydraulic cylinder (Pa), d_{cy} is the hydraulic cylinder's inner diameter (m), δ_{cy} is the clearance width between the piston and the cylinder wall of the hydraulic cylinder (m), and l_{cy} is the clearance length (m).

3.3.3. Thermal Power Model of the Hydraulic Accessories

The thermal power generated by the pressure loss of oil flowing through the hydraulic pipeline can be expressed as:

$$P_{sp} = q\left(\sum_{i=1}^{n}\frac{40 l_{pi}\rho_0 \nu v_{pi}}{d_{pi}^2} + \sum_{j=1}^{m}\xi_j\frac{\rho_0 v_{pj}^2}{2}\right) \tag{7}$$

where P_{sp} is the thermal power loss of hydraulic pipeline (W), q is the main oil circuit flow (m^3/s), d_{pi} is the hydraulic diameter of each pipeline (m), l_{pi} is the length of each pipe (m), ρ_0 is the hydraulic oil density (kg/m^3), v is the hydraulic oil kinematic viscosity (m^2/s), v_{pi} is the average flow velocity of oil in each pipeline (m/s), ξ_j is the local loss coefficient of each bend pipeline, and v_{pj} is the average flow velocity of oil in each bend pipeline (m/s).

The thermal power generated by the pressure loss of oil flowing through the valve block can be expressed as:

$$P_{vb} = q\left(\sum_{i=1}^{n}\frac{75 l_{hi}\rho_0 \nu v_{hi}}{2d_{hi}^2} + k_y q\right) \tag{8}$$

where P_{vb} is the heat power loss of valve block (W), l_{hi} is the length of each channel (m), v_{hi} is the average flow velocity of oil in each channel (m/s), d_{hi} is the hydraulic diameter of each channel (m), and k_y is the hydraulic component pressure factor.

The heat production of hydraulic valve is mainly caused by the throttling loss, and the power loss of the hydraulic valve can be expressed as:

$$P_v = \Delta p_v q_v \tag{9}$$

where P_v is the thermal power loss of the hydraulic valve (W), Δp_v is the pressure drop after the oil flows through the hydraulic valve (Pa), and q_v is the flow through the hydraulic valve (m^3/s).

3.4. Solution of CHS Thermal Power

In order to study the heat generation power and heating law of the CHS, Matlab/Simulink was used to build the heat generation model, as shown in Figure 4.

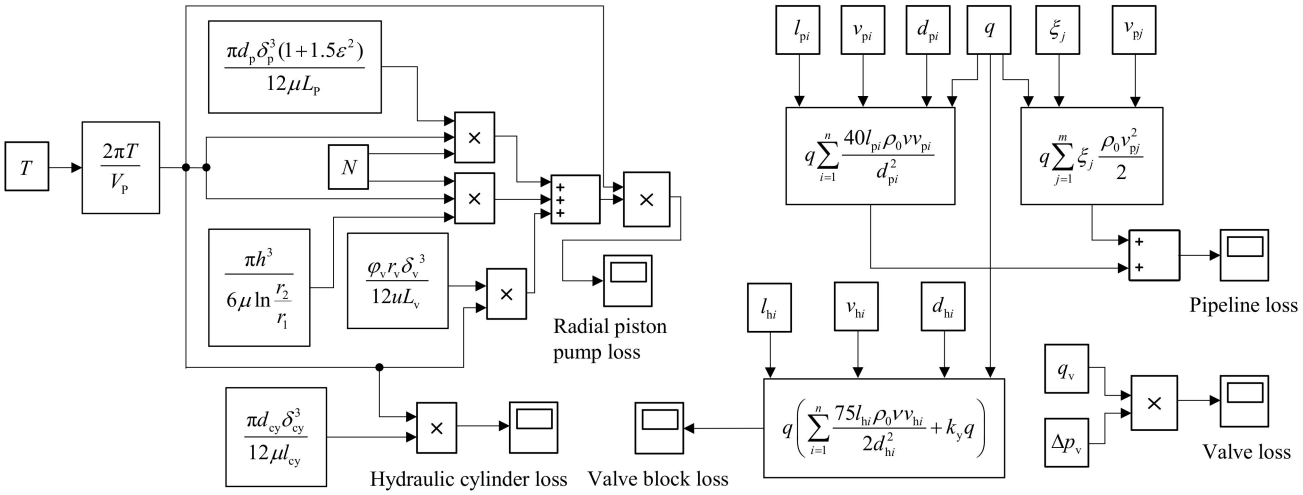

Figure 4. Thermal power model of the closed hydraulic system (CHS).

The basic parameters of the radial piston pump are shown in Table 3.

Table 3. Radial piston pump parameters.

Parameters	Value
Piston diameter (m)	0.011
Clearance between piston and inner wall of the rotor piston bore (m)	2×10^{-5}
Oil dynamic viscosity (Pa·s)	3.6×10^{-2}
Contact length between piston and cylinder bore (m)	0.03
Thickness of oil film between stator and sliding shoe (m)	1.5×10^{-5}

The heat generation power of each part in the CHS under different torques is shown in Table 4.

Table 4. Heat generation power of each part in the CHS under different torques.

Torque (Nm)	Radial Piston Pump (W)	Hydraulic Cylinder (W)	Accessories (W)
0	0.00	0.00	0.00
10	12.2	3.32	2.62
20	35	11.14	4.80
28	53	18.04	6.11

3.5. Thermal Power Analysis of the EHSPCS

Through the analysis of the previous thermal power model, the heat generation power of the PMSM and CHS at 0 Nm, 10 Nm, 20 Nm, and 28 Nm were obtained. In order to facilitate comparison and observation, the thermal power loss of each part in the EHSPCS under different torques is plotted as a line graph in Figure 5.

Figure 5 shows that, as the load increases, the current of the PMSM coil increases, and the copper loss becomes larger and larger, resulting in a power loss much higher than that of other parts, and its heating ratio is above 77% under all working conditions. The second heat source is the radial piston pump, which accounts for 15.7% of the total power loss when fully loaded. The power loss of hydraulic cylinders and accessories accounted for less than 6%. Therefore, it can be seen that, when the EHSPCS works at a high torque, the

PMSM and hydraulic pump temperature can be optimized to achieve the normal operation of the system.

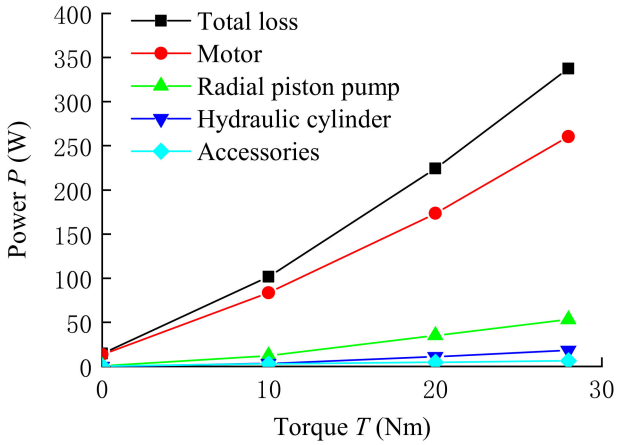

Figure 5. Thermal power loss of the EHSPCS under different torques.

4. Research on the Thermal Balance Temperature Field

System thermal balance analysis refers to calculating the total heat generation power and heat dissipation power of all components of the system. When the total heat generation power and total heat dissipation power of the system reach dynamic balance, the final steady-state temperature of each component of the system is solved.

In this study, the steady state temperature of the PMSM under different working conditions in ANSYS software (Canonsburg, PA, USA) was imported into the AMESim model of the CHS. PMSM temperature was used as input of external heat of the CHS, and the steady state temperature of the CHS was obtained through simulation, and then the steady state temperature of the CHS is imported into the PMSM model for heat balance simulation again, and the simulated temperature is imported into the CHS model again. After several repeated iterations, the heat balance temperature of the EHSPCS is finally obtained.

4.1. Thermal Balance Analysis of the PMSM Temperature Field

There are many heat sources in a PMSM, including stator cores, rotor cores, windings, and permanent magnets. Part of the heat generated is transferred to the shell through the air gap, and then convectively exchanged between the shell and the air; the other part directly contacts the air through the end face of the heat source [29]. It can be seen that the heat transfer is quite complicated. In this study, in order to improve the efficiency and accuracy of the solution, the finite element method was adopted to analyze the thermal balance of the temperature field of the motor.

4.1.1. Establishment of the PMSM Temperature Field Model

In this study, the PMSM is the axial motor, and both sides of the motor are symmetrical about the axial center plane, so the 1/2 model was selected with the axial center plane as the boundary. Since this motor is evenly distributed in the circumferential direction, the 1/4 model is taken in the circumferential direction. A three-dimensional temperature field analysis model was established using ANSYS Workbench software, as shown in Figure 6.

In order to facilitate the solution, the following assumptions are made for the temperature field analysis model of the PMSM:

(1) The internal temperature field of the PMSM is continuous along the circumference and axial direction.
(2) The influence of the winding skin effect is ignored.

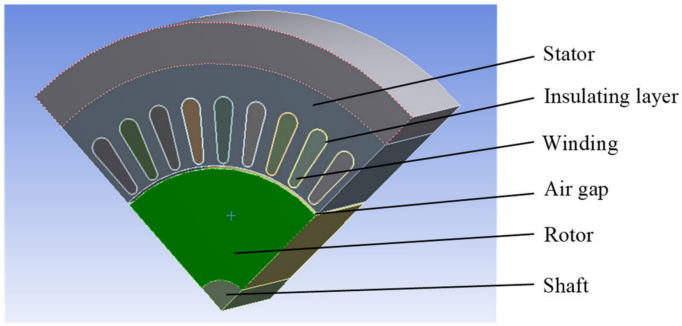

Figure 6. Three-dimensional analysis model of the PMSM's temperature field.

4.1.2. Calculation of the PMSM Temperature Field Parameters

A PMSM has many heat generating parts and complex heat transfer methods, but heat dissipation is carried out by convection heat dissipation or radiation heat dissipation through the shell and the outside. Compared with convection heat dissipation, radiation heat dissipation is very small. Therefore, when solving the PMSM temperature field, only two heat dissipation methods, thermal conduction and thermal convection, need to be calculated.

The heat transfer process of the internal temperature field of the motor can be expressed as:

$$\begin{cases} \lambda \frac{d^2t}{dx^2} = c\rho_m \frac{dt}{d\tau} \\ \lambda_s \frac{dt}{dn} \Big| S_1 = 0 \\ \lambda_s \frac{dt}{dn} \Big| S_2 = -\alpha(t - t_e) \end{cases} \tag{10}$$

where λ is the thermal conductivity of various parts of the motor (W/(m °C)), t is the temperature (°C), c is the material specific heat capacity (J/(kg °C), ρ_m is the material density (kg/m^3), τ is the time constant (s), λ_s is the normal thermal conductivity of the adiabatic surface and the heat dissipation surface (W/(m °C)), S_1 is the motor adiabatic boundary surface, S_2 is the motor heat dissipation boundary surface, α is the convective heat transfer coefficient of the heat dissipation surface (W/(m^2 °C)), and t_e is the temperature of the ambient medium around the heat dissipation surface (°C).

First of all, it is necessary to give initial conditions to the three-dimensional PMSM temperature field model. In this study, the initial ambient temperature is set to 25 °C. Secondly, it is necessary to assign boundary conditions to the model. According to the first formula of Equation (10), the thermal conductivity boundary conditions can be set by assigning the thermal conductivity of the various components of the motor. The second formula in Equation (10) is the adiabatic boundary condition, as shown in Figure 7, assuming that the A, B and C planes are all symmetry planes, which are the adiabatic planes in this study. The third formula in Equation (10) is the boundary condition of convection heat dissipation, which includes the stator winding, stator core, rotor core, shell, and permanent magnet contact surface with the air gap and outside atmosphere.

The calculation of the equivalent thermal conductivity of the stator winding is to equate the copper wire in the stator slot as a whole piece of copper conductor. The slot insulation and dipping varnish are equivalent to the ring-shaped insulating layer, and the thermal conductivity of the equivalent insulating layer can be expressed as:

$$\lambda_{\text{eq}} = \frac{\sum_{i=1}^{n} \delta_i}{\sum_{i=1}^{n} \frac{\delta_i}{\lambda_i}} \tag{11}$$

where λ_{eq} is the equivalent thermal conductivity (W/(m °C)), δ_i is the thickness of each thermal conductor (m), and λ_i is the thermal conductivity of each thermal conductor (W/(m °C)).

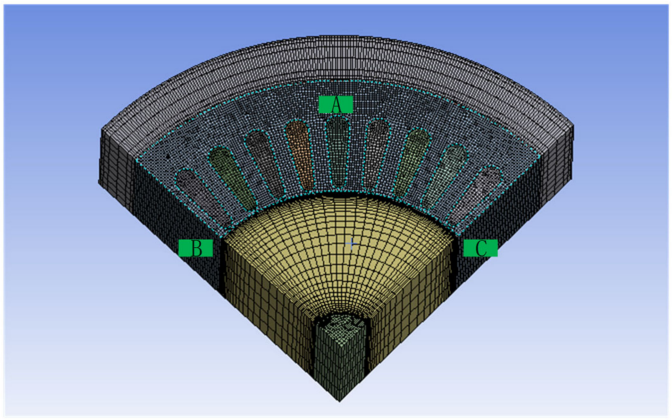

Figure 7. PMSM temperature field boundary condition. Plane A, B and C are all adiabatic surfaces.

According to the installation characteristics of the stator core, insulating varnish is applied between the layers, so the thermal conductivity between the layers is relatively small. This direction is set as the z-direction; the other two directions perpendicular to the z-direction are set to the x-direction and y-direction.

Through calculation and product samples, the thermal conductivity and specific heat capacity of each part in the PMSM in this study are shown in Table 5.

Table 5. Physical properties of PMSM materials.

Materials	Equivalent Thermal Conductivity (W/(m °C))	Specific Heat Capacity (J/(kg °C))
Stator core x-direction	40	465
Stator core y-direction	40	465
Stator core z-direction	0.95	465
Rotor core	45	445
Stator winding	378	380
Permanent magnet	8.9	386
Air gap	0.03	1000
Shaft	43	460
Motor casing	237.5	900
Insulating layer	0.18	1700

The convective heat transfer coefficient between the end face of the stator core and the rotor core and the air inside the motor can be expressed as:

$$a = (1 + 0.25v_m)/0.045 \tag{12}$$

where v_m is the wind speed inside the motor (m/s).

Assuming that the initial air temperature on the housing surface is atmospheric temperature, the convective heat transfer coefficient on the housing surface can be expressed as:

$$\alpha = \alpha_0(1 + k_1\sqrt{v_w})^3\sqrt{\frac{\theta}{25}} \tag{13}$$

where α_0 is the convective heat transfer coefficient of the heating surface of the object in the air, k_1 is the air blowing efficiency coefficient, v_w is the outer surface wind speed (m/s and θ is the outer wall temperature of the motor casing (°C).

The convective heat transfer coefficient of the stator core end face, rotor core end face, and the outer surface of the casing are shown in Table 6 under the natural cooling conditions of the motor.

Table 6. Convective heat transfer coefficient of different parts in the PMSM.

Parts	Convective Heat Transfer Coefficient (W/(m^2 °C))
Stator core end face	22.22
Rotor core end face	22.22
Outer surface of motor casing	12.22

The convective heat transfer coefficient of the housing surface under different wind speeds is shown in Table 7.

Table 7. Convective heat transfer coefficient of the housing surface under different wind speeds.

Wind Speeds (m/s)	Convective Heat Transfer Coefficient (W/(m^2 °C))
1	12.22
3	22.80
5	25.88

4.1.3. Thermal Balance Analysis of the PMSM in Natural Cooling

In order to explore the influence of the load torque on temperature rise, the temperature field of the PMSM with different loads of 0 Nm, 10 Nm, 20 Nm, and 28 Nm was simulated and analyzed under a constant speed of the PMSM (500 r/min).

A 3D model was built with SolidWorks software (Waltham, MA, USA), and it was then imported into ANSYS and meshed, and it was finally imported into Fluent. According to the PMSM temperature field parameters obtained above, the energy equation was turned on, the boundary conditions and heat source were set, and the temperature field of the PMSM under different loads was simulated. When the residual error was observed to converge to the final setting error, temperature field-distributed cloud images of the PMSM under different loads were obtained, as shown in Figure 8. The simulation time is 360 min.

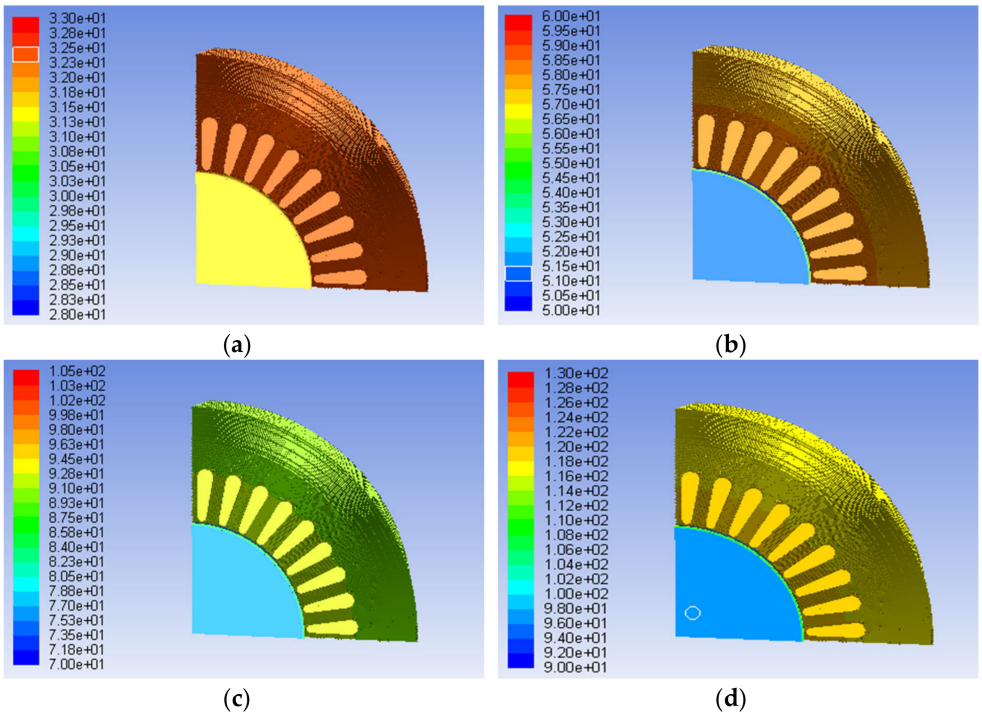

Figure 8. Temperature field-distributed cloud images of the PMSM under different loads: (**a**) 0 Nm load; (**b**) 10 Nm load; (**c**) 20 Nm load; (**d**) 28 Nm load.

The temperature curve of each part in the PMSM under different loads is shown in Figure 9.

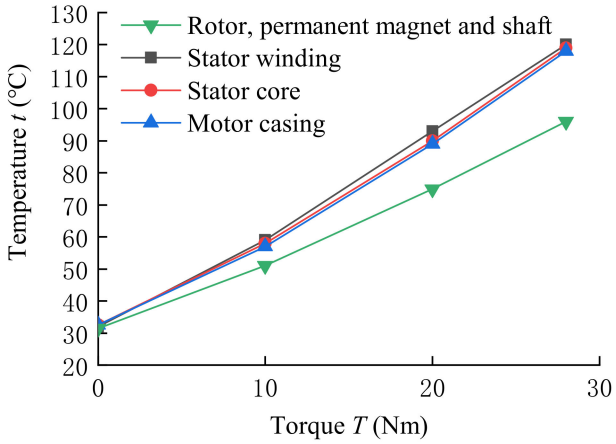

Figure 9. The temperature of each part in the PMSM under different loads.

It can be seen in Figure 9 that the temperature of the stator winding, stator core, and motor casing are relatively close. This is because the stator winding and the stator core themselves generate a high amount of heat, and the stator core and the motor casing are in an interference fit, so the temperature difference between the three is very small, and the maximum temperature under rated conditions is 120 °C. The temperature of the rotor, permanent magnets, and shaft is relatively low, and its heat is mainly transferred from the stator winding and the stator core through the air gap. The maximum temperature under rated conditions is 96 °C.

4.1.4. Thermal Balance Analysis of the PMSM in Forced Wind Cooling

Under the condition of the same load torque and rotation speed, compared with natural cooling, the thermal balance analysis of the temperature field under forced wind cooling is only different in the convective heat transfer coefficient of the motor casing surface. Steady-state temperature field-distributed cloud images are shown below. The cross-sectional area of the fan is the same, and the PMSM operates at a constant speed (500 r/min) under different loads of 0 Nm, 10 Nm, 20 Nm, and 28 Nm and at wind speeds of 1 m/s, 3 m/s, and 5 m/s in Figures 10–12, respectively.

It can be seen in Figures 10–12 that the temperature of each part in the PMSM has been reduced under forced wind cooling. The stator winding is still the main heat source when loaded. For observation and analysis, the temperature curves of the stator windings under different wind speeds and loads are shown in Figure 13.

It can be seen in Figure 13 that the greater the load torque of the system, the more obviously the increase in wind speed reduces the temperature of the stator winding. At the rated load of 28 Nm, the temperature difference between adjacent wind speed stator windings at 0 m/s, 1 m/s, 3 m/s, and 5 m/s is 14 °C, 9 °C, and 4.5 °C, respectively. Therefore, with the increase of wind speed, the gradient of system temperature decline is gradually decreasing, and a higher wind speed does not necessarily lead to an improvement. When the wind speed reaches a certain value, the value of the system temperature may be small, and the benefit is very low.

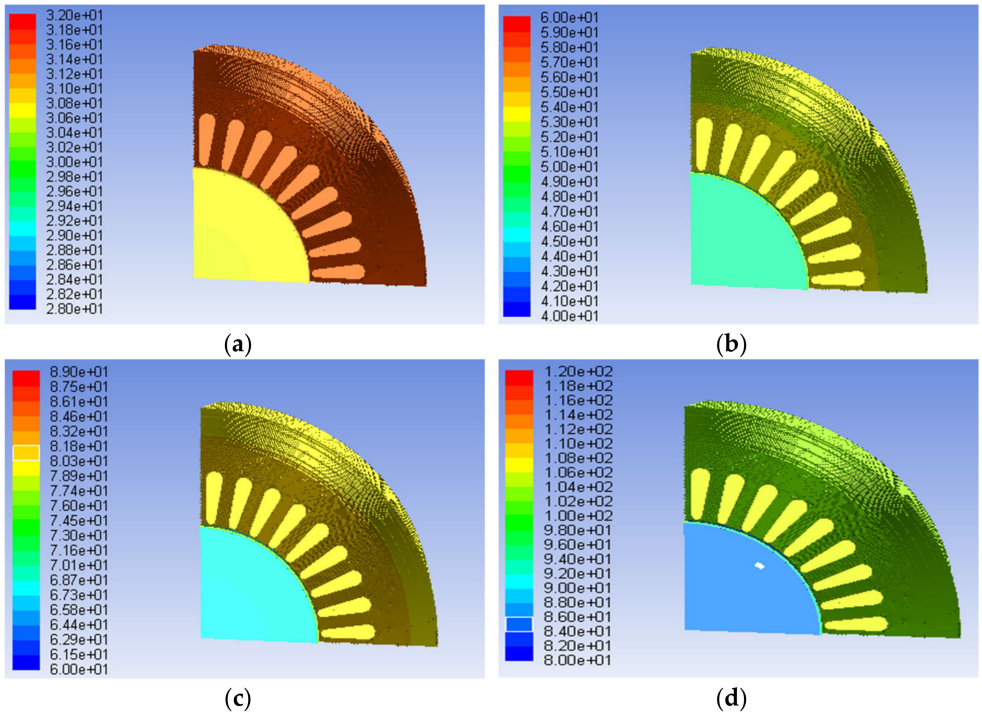

Figure 10. Temperature field-distributed cloud image of the PMSM under different loads at a 1 m/s wind speed: (**a**) 0 Nm load; (**b**) 10 Nm load; (**c**) 20 Nm load; (**d**) 28 Nm load.

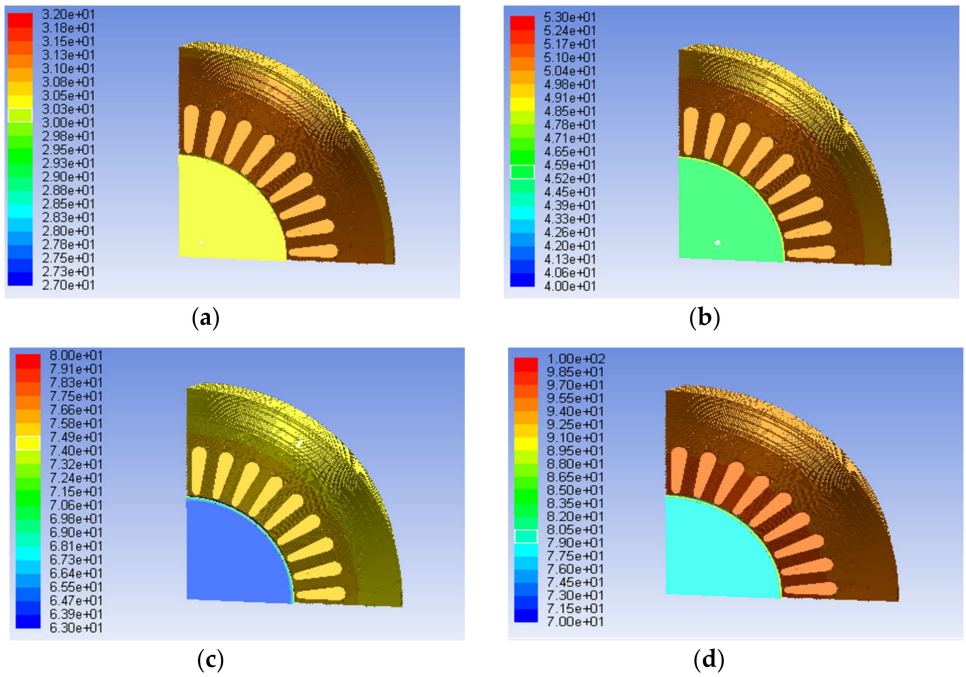

Figure 11. Temperature field-distributed cloud image of the PMSM under different loads at a 3 m/s wind speed: (**a**) 0 Nm load; (**b**) 10 Nm load; (**c**) 20 Nm load; (**d**) 28 Nm load.

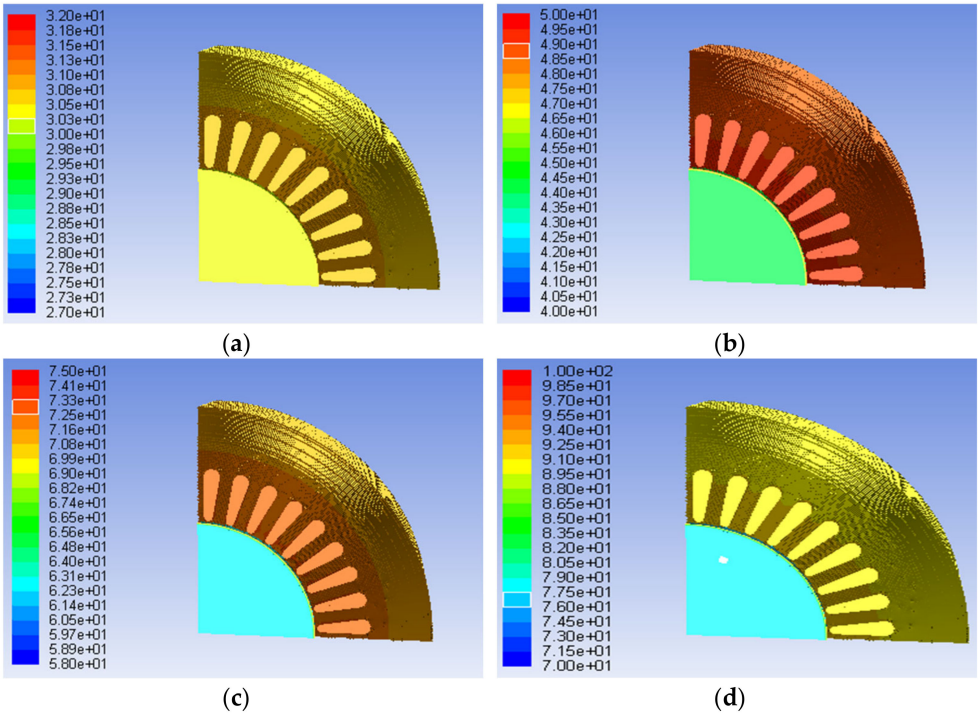

Figure 12. Temperature field-distributed cloud image of the PMSM under different loads at a 5 m/s wind speed: (**a**) 0 Nm load; (**b**) 10 Nm load; (**c**) 20 Nm load; (**d**) 28 Nm load.

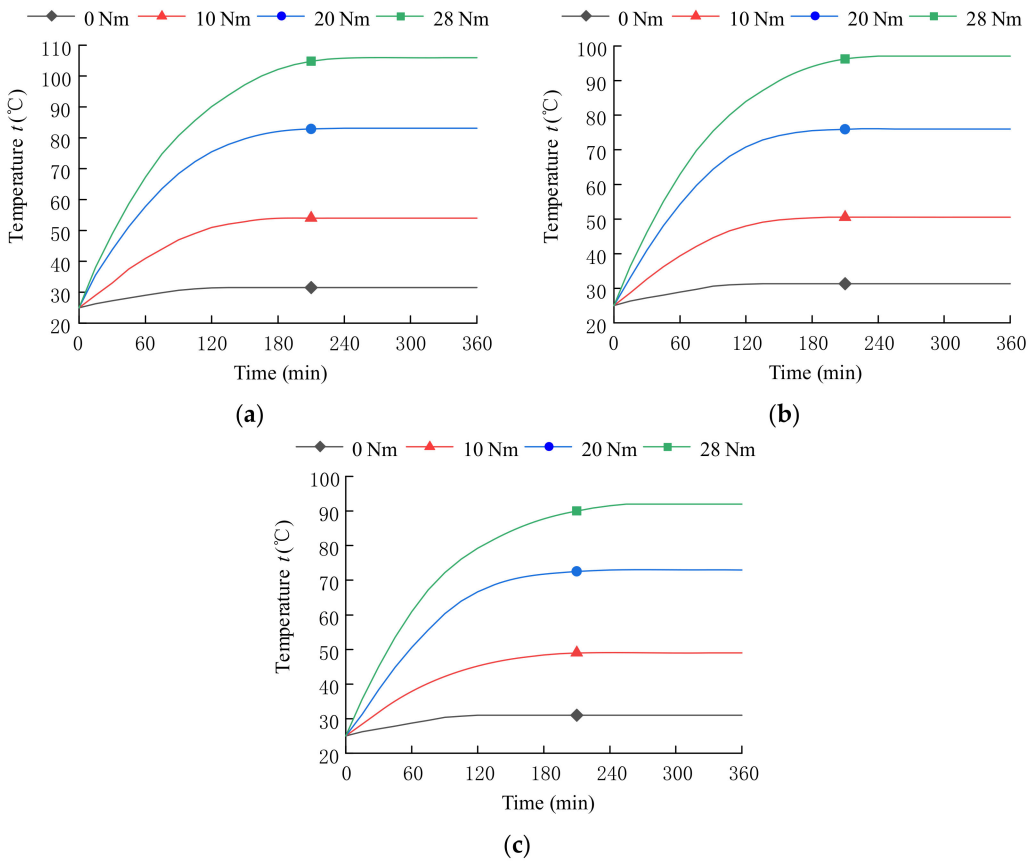

Figure 13. Temperature curves of stator windings under different wind speeds and loads: (**a**) 1 m/s wind speed; (**b**) 3 m/s wind speed; (**c**) 5 m/s wind speed.

4.2. Thermal Balance Analysis of the CHS

In the EHSPCS, the PMSM and the radial piston pump are in direct contact, and there must be a temperature difference between them, resulting in thermal conduction. The thermal-hydraulic modeling architecture of the CHS is shown in Figure 14.

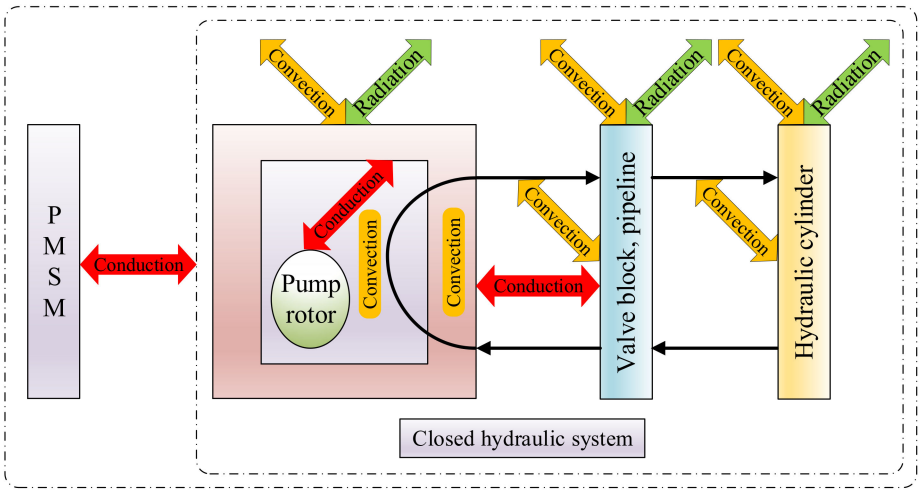

Figure 14. Thermal-hydraulic modeling architecture of the CHS.

Based on the previous analysis, the heat of the radial piston pump mainly comes from leakage heat. Part of this heat is carried by the oil to the valve block, pipeline, and hydraulic cylinder, and part of the heat is convectively heat exchanged with the rotor and shell through the oil. The heat of the rotor conducts thermal conduction with the shell, and finally uniformly dissipates into the air through the thermal convection and thermal radiation of the shell. Part of the heat is transferred to the valve block through thermal conduction. The valve blocks, pipelines, and hydraulic cylinders placed in the atmosphere transfer heat by convection and radiation with the air. Due to the complicated heat exchange form of the system, AMESim software was used in this study to analyze the thermal balance of the temperature field of the CHS.

4.2.1. Establishment of the CHS Simulation Model

The simulation model of the CHS is shown in Figure 15.

The parameters of the CHS simulation model are shown in Table 8.

Table 8. Parameters of the CHS simulation model.

Parameters	Value
Oil	L-HM46
Rotor mass (kg)	1.7
Piston pump housing mass (kg)	2.5
Valve block mass (kg)	40
Total thermal dissipation area of valve block (m^2)	0.2
Thermal conduction area of valve block (m^2)	0.04
Thermal dissipation area of piston pump housing (m^2)	0.55
Cooling area of hydraulic cylinder (m^2)	0.3
Hydraulic cylinder diameter (m)	0.05
Hydraulic cylinder rod diameter (m)	0.03
Hydraulic cylinder stroke (m)	0.1
Pressure relief valve setting pressure (bar)	250
Check valve opening pressure (bar)	0.25
Outside temperature under natural conditions (°C)	25

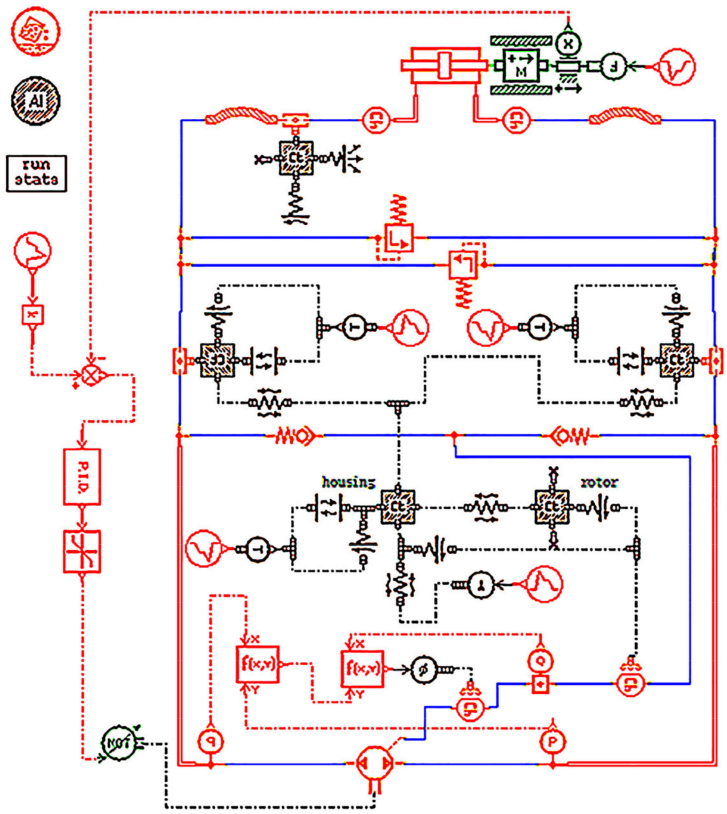

Figure 15. Simulation model of the CHS.

4.2.2. Thermal Balance Analysis of the CHS under PMSM Natural Cooling

Since the heat of the system hydraulic accessories is smaller than that of the radial piston pump, the power loss of the pipeline, valve block, and valve is equivalent to the power loss of the hydraulic cylinder, which is collectively referred to as the power loss of the hydraulic cylinder. AMESim simulation software was used to calculate the heat generation power and heat dissipation power of each part of the system under the PMSM's natural cooling conditions under different torques, as shown in Figure 16.

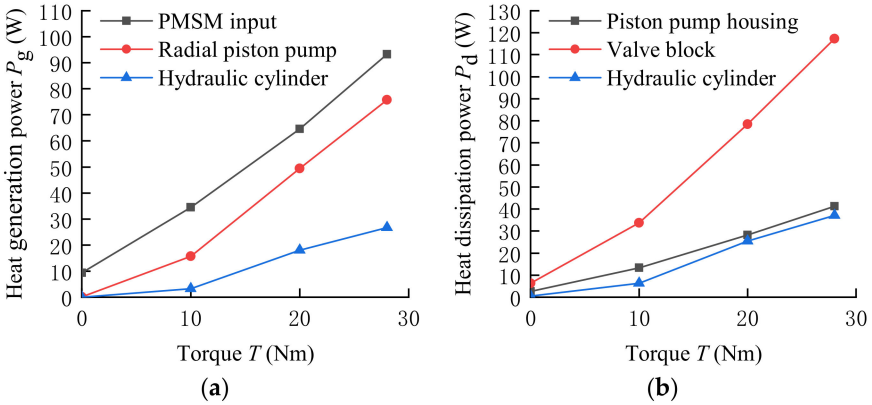

Figure 16. Heat generation power and heat dissipation power of each part in CHS under different torques: (**a**) heat generation power; (**b**) heat dissipation power.

Figure 16a shows that the greatest amount of heat is conducted by the PMSM to the CHS, followed by the radial piston pump and lastly the hydraulic cylinder. Figure 16b shows that the heat dissipation power of the valve block is the largest, which is because the heat dissipation area of the valve block is larger than that of the radial piston pump.

The hydraulic cylinder has the lowest heat dissipation power because its temperature is lower than that of the former two.

When the heat dissipation power of the system is equal to the heat generation power, the system reaches thermal balance. The thermal balance temperature of each component in the CHS under different torques under the PMSM's natural cooling conditions is shown in Figure 17.

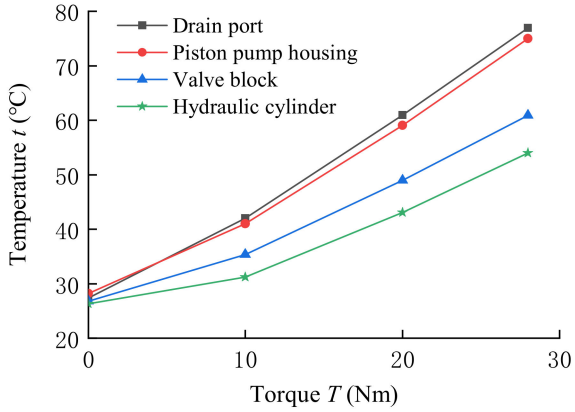

Figure 17. Thermal balance temperature of each part in CHS under different torques.

Figure 17 shows that the greater the torque, the higher the thermal balance temperature of each part of the system. In the presence of load, the temperature of the drain port of the radial piston pump has always been at a maximum, and the oil temperature exceeds the ideal value of 60 °C at the load of 20 Nm.

4.2.3. Thermal Balance Analysis of the CHS under PMSM Forced Wind Cooling

The motor casing temperature under the forced wind cooling of the PMSM was imported into the AMESim simulation model. The heat generation power and heat dissipation power of each component in the CHS were obtained under the wind speeds of 1 m/s, 3 m/s, and 5 m/s and at different load conditions, as shown in Figures 18–20, respectively.

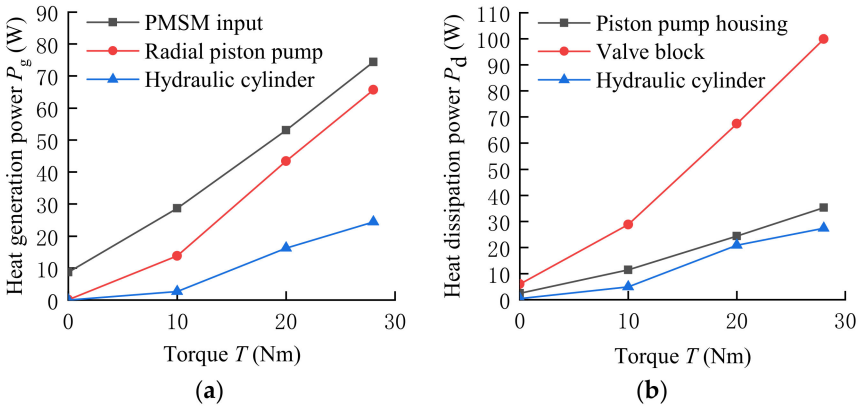

Figure 18. Heat production power and heat dissipation power of each component under different load conditions at a 1 m/s wind speed: (**a**) heat generation power; (**b**) heat dissipation power.

Figures 18–20 show that, as the wind speed increases, the thermal power input to the CHS by the PMSM decreases, which in turn reduces the thermal balance temperature of the CHS. The thermal balance temperature of each part in the CHS under different load conditions of 1 m/s, 3 m/s, and 5 m/s is shown in Figure 21.

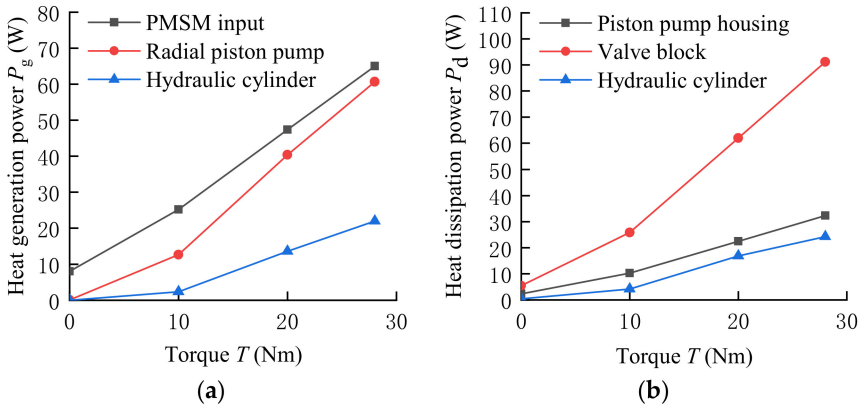

Figure 19. Heat production power and heat dissipation power of each component under different load conditions at a 3 m/s wind speed: (**a**) heat generation power; (**b**) heat dissipation power.

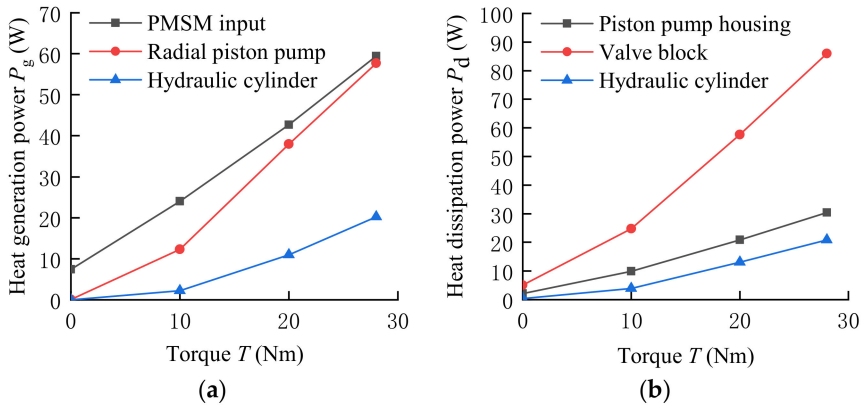

Figure 20. Heat production power and heat dissipation power of each component under different load conditions at a 5 m/s wind speed: (**a**) heat generation power; (**b**) heat dissipation power.

Figure 21 shows that the greater the load torque of the system, the more obviously the increase in wind speed reduces the temperature of the CHS. The drain port temperature of the radial piston pump is always at a maximum, but when the load is 20 Nm, the drain port temperature does not exceed 60 °C. When the load is 28 Nm, the drain port temperature is between 60 °C and 70 °C.

4.3. Thermal Balance Analysis of the EHSPCS

According to the thermal balance analysis of the temperature field for the PMSM and the CHS above, the stator winding is the PMSM component with the highest temperature, and the drain port is the CHS component with the highest temperature. If the PMSM works under a rated load with natural cooling, its steady-state temperature is likely to exceed its alarm value, and the temperature of the CHS will exceed 60 °C, which will seriously affect the service life of the system. Therefore, in this study, the ideal rated load of the system was decided to be 2/3 of the highest load, i.e., 18 Nm. In this case, the temperature of the stator winding is about 80 °C, and the temperature of the drain port is not more than 60 °C.

The load torque of the servo motor can be expressed as:

$$T = \Delta pV \tag{14}$$

$$\Delta p = \frac{F}{A} \tag{15}$$

where T is the servo motor torque (Nm), F is the external load force of the hydraulic cylinder (N), V is the radial piston pump displacement (m^3/rad), and A is the effective area of the hydraulic cylinder (m^2).

Equations (14) and (15) show that the load torque of the motor can be reduced by choosing hydraulic pump with small displacement, and the pressure of the system can be reduced by increasing the effective working area of the hydraulic cylinder or by using two cylinders in parallel connection. If the system is limited by space, forced wind cooling can be done to reduce the temperature of the PMSM. In the PMSM selection process, the rated power, cooling method, and wind speed should be appropriately selected according to the external load and the temperature to be controlled.

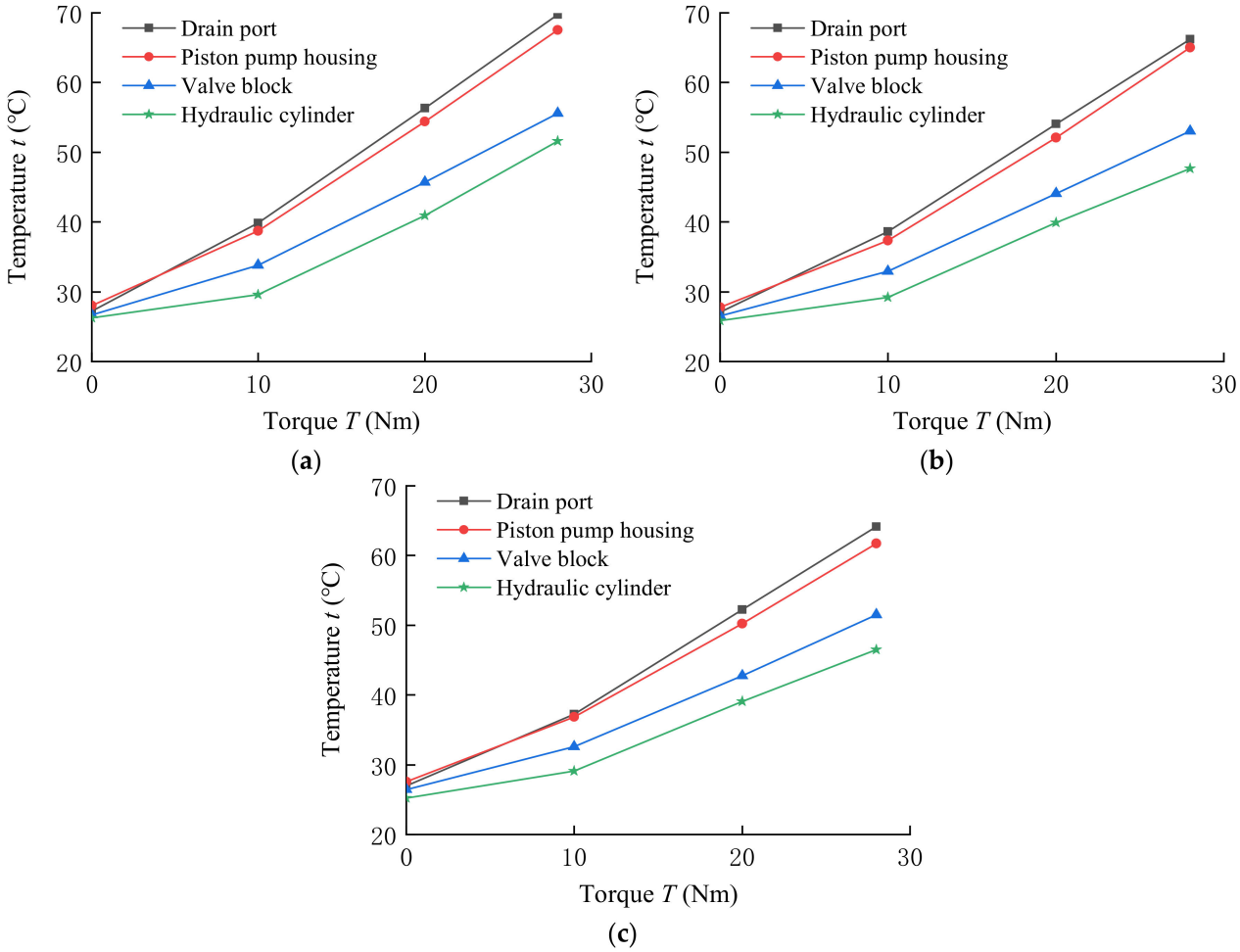

Figure 21. The thermal balance temperature of each component of the CHS under different wind speeds and torques: (**a**) 1 m/s wind speed; (**b**) 3 m/s wind speed; (**c**) 5 m/s wind speed.

5. Experimental Verification

The thermal balance of the temperature field of the EHSPCS under constant speed and typical working conditions was tested and verified (500 r/min). By comparing the test results with the theoretical solution results, the correctness of the analysis method for the thermal balance of the temperature field of the EHSPCS was verified.

5.1. Introduction of the EHSPCS Experimental Platform

The experimental platform of the EHSPCS is shown in Figure 22, including a power unit and an execution unit.

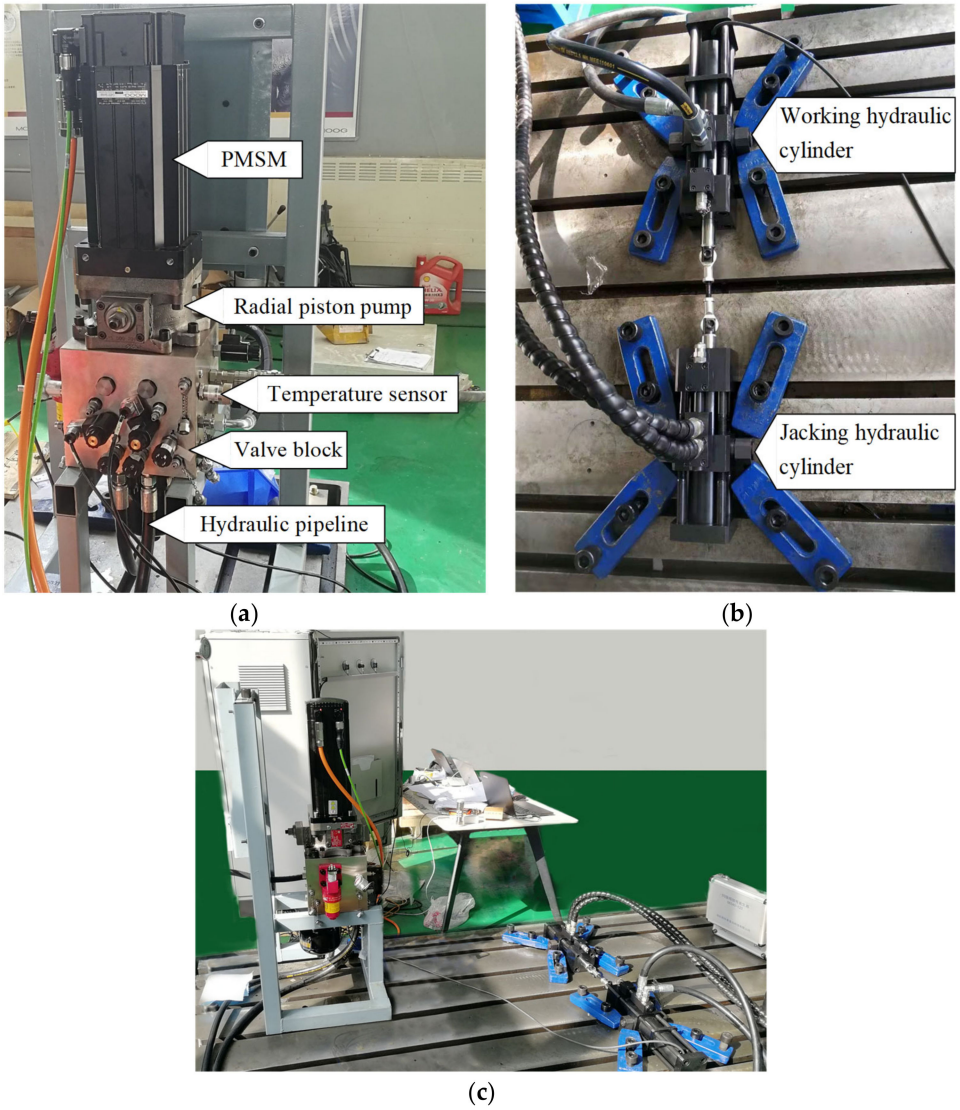

Figure 22. Experimental platform of the EHSPCS: (**a**) power unit; (**b**) execution unit; (**c**) test bench.

The working hydraulic cylinder and the power unit are connected by hydraulic pipelines. A jacking hydraulic cylinder and a working hydraulic cylinder are opposite to each other to provide a constant load for the system. The EHSPCS entails a working hydraulic cylinder in a static and jacking state. Once the thermal balance of the system is stable, the thermal balance temperature of the EHSPCS can be measured under different loads and under natural cooling and forced wind cooling. The PMSM has its own winding temperature detection device, and the CHS is equipped with an external threaded temperature sensor at the drain port, which can detect the temperature at the drain port in real time.

5.2. System Temperature Rise Experiment under PMSM Natural Cooling

In this experiment, by changing the output force of the jacking hydraulic cylinder, loads with torques of 0 Nm, 10 Nm, 20 Nm, and 28 Nm were added, respectively. The simulation and experimental temperature rise comparisons of the stator winding and the drain port under different loads are shown in Figure 23.

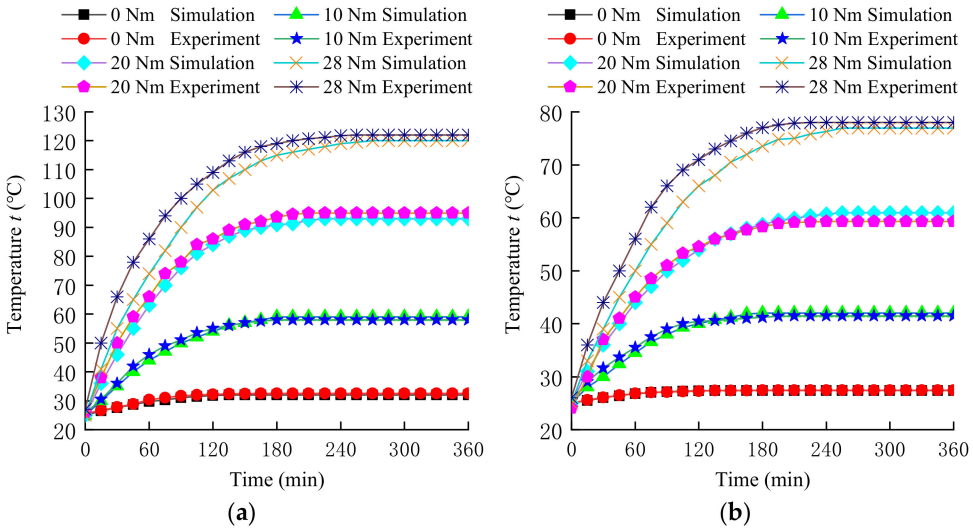

Figure 23. Simulation and experimental temperature rise comparison of stator windings and drain ports under different loads when PMSM is natural cooling: (**a**) stator winding temperature rise comparison; (**b**) drain port temperature rise comparison.

Figure 23 shows that the simulation and experimental temperature rise curves of the stator winding and the drain port under different loads basically coincide, and the temperature rise curves are all rising smoothly. The steady-state temperature reached is basically the same.

5.3. System Temperature Rise Experiment under PMSM Forced Wind Cooling

In this study, an fan was used for forced wind cooling for the PMSM. The simulation and experimental temperature rise comparison curves of the stator winding and the drain port were obtained under the wind speeds of 1 m/s, 3 m/s, and 5 m/s and under different load conditions, as shown in Figures 24–26, respectively.

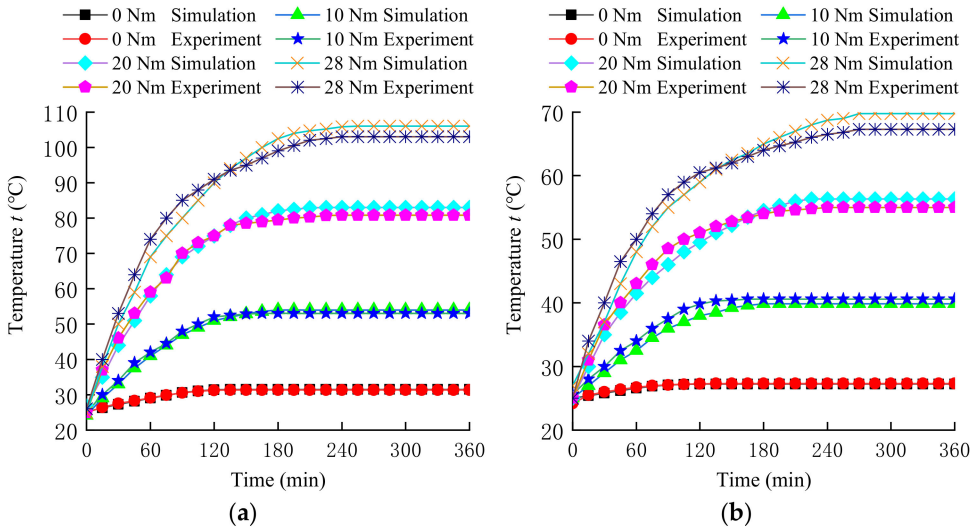

Figure 24. Simulation and experimental temperature rise comparison of the stator winding and the drain port under different load conditions at a 1 m/s wind speed: (**a**) stator winding; (**b**) drain port.

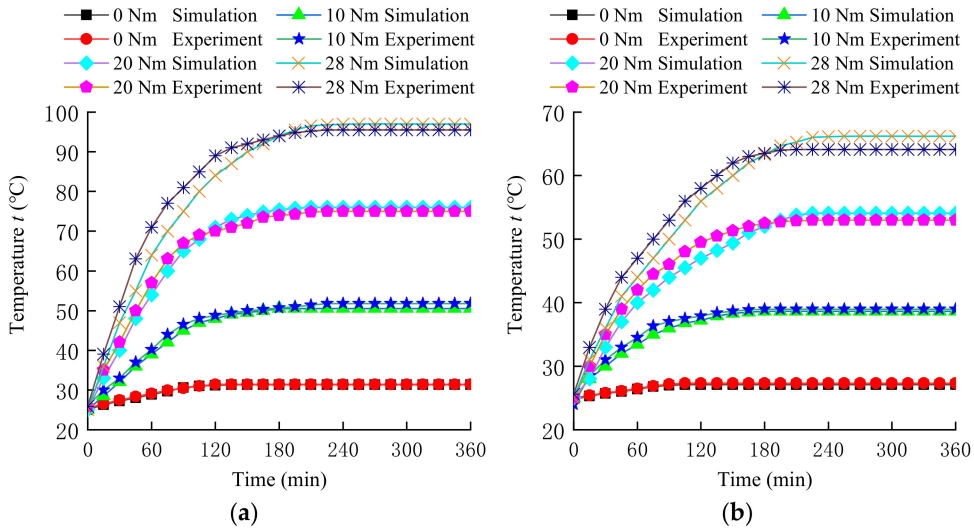

Figure 25. Simulation and experimental temperature rise comparison of the stator winding and the drain port under different load conditions at a 3 m/s wind speed: (**a**) stator winding; (**b**) drain port.

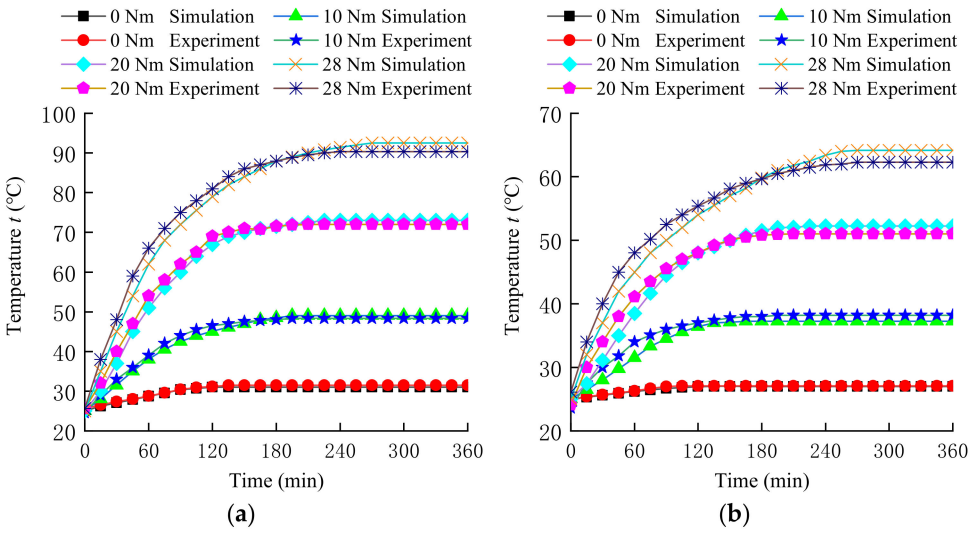

Figure 26. Simulation and experimental temperature rise comparison of the stator winding and the drain port under different load conditions at a 5 m/s wind speed: (**a**) stator winding; (**b**) drain port.

Figures 24–26 show that the simulation curve and the experimental curve basically coincide. With the increase in fan speed, the steady-state temperature under different loads also decreases. The maximum difference between the simulation and the experimental temperature does not exceed 3 °C, which is within the allowable deviation range.

In summary, the deviation between the simulation value and the experimental value of the EHSPCS under natural cooling and forced air cooling is not more than 3 °C, which basically verifies the effectiveness of the thermal balance analysis method of the temperature field of the EHSPCS.

6. Conclusions

In this paper, a method of thermal balance analysis of the EHSPCS under different loads and different wind speeds is presented. The thermal power model of the EHSPCS was established. The analysis shows that the power loss of the PMSM's stator winding is the largest, and its heating proportion is above 77% under all working conditions. The second heat source, the radial piston pump, accounts for 15.7% of the total power loss at full load. The PMSM's stator winding has the highest temperature. With the increase in

system load torque, the increase in wind speed more obviously reduces the temperature of stator winding; however, with the increase in wind speed under the same torque, the gradient of system temperature decline is gradually decreasing, and a higher wind speed does not necessarily lead to an improvement. The PMSM's conduction primarily explains the temperature rise of the CHS; the heat production of the radial piston pump plays a smaller role. The drain port temperature of the radial piston pump is the highest of the CHS. The higher the load torque is, the higher the heat balance temperature will be, and the PMSM's forced wind cooling will cause the temperature of the drain port to decrease. In this study, the ideal rated load of the system is 2/3 of the highest load, i.e., 18 Nm. The heat balance temperature of the EHSPCS can be reduced by, e.g., choosing hydraulic pump with small displacement, connecting tow cylinders in parallel, forcing air cooling, or increasing the area of hydraulic cylinder under considering the relationship between pressure and flow comprehensively. Heat balance optimization can be achieved by adding built-in cooling devices such as cooling fans to the PMSM. The temperature rise experiments of the EHSPCS under natural cooling and forced wind cooling were carried out, and the correctness of the temperature field obtained by the thermal balance analysis method was verified by comparison with simulation results, which provides a reference for the design of PMSM cooling device and the selection of components.

Author Contributions: Formal analysis, B.Y.; Funding acquisition, Z.J.; Methodology, G.Y., Z.J. and M.Y.; Project administration, B.Y.; Resources, G.Y.; Software, B.Y.; Supervision, M.Y.; Validation, G.Y. and Z.J.; Writing—original draft, G.Y.; Writing—review & editing, M.Y. All authors have read and agreed to the published version of the manuscript.

Funding: This research was supported by the Key R&D Projects in Hebei Province (No. 20314402D) and the Key Project of Science and Technology Research in Hebei Province (No. ZD2020166).

Institutional Review Board Statement: Not applicable.

Informed Consent Statement: Not applicable.

Data Availability Statement: Not applicable.

Conflicts of Interest: The authors declare no conflict of interest.

References

1. Yu, B.; Wu, S.; Jiao, Z.; Shang, Y. Multi-Objective Optimization Design of an Electrohydrostatic Actuator Based on a Particle Swarm Optimization Algorithm and an Analytic Hierarchy Process. *Energies* **2018**, *11*, 2426. [CrossRef]
2. Song, B.; Lee, D.; Park, S.Y.; Baek, Y.S. Design and Performance of Nonlinear Control for an Electro-Hydraulic Actuator Considering a Wearable Robot. *Processes* **2019**, *7*, 389. [CrossRef]
3. Nguyen, M.T.; Dang, T.D.; Ahn, K.K. Application of Electro-Hydraulic Actuator System to Control Continuously Variable Transmission in Wind Energy Converter. *Energies* **2019**, *12*, 2499. [CrossRef]
4. Chakraborty, I.; Mavris, D.N.; Emeneth, M.; Schneegans, A. A methodology for vehicle and mission level comparison of More Electric Aircraft subsystem solutions: Application to the flight control actuation system. *Proc. Inst. Mech. Eng. Part G Aerosp. Eng.* **2015**, *229*, 1088–1102. [CrossRef]
5. Alle, N.; Hiremath, S.S.; Makaram, S.; Subramaniam, K.; Talukdar, A. Review on electro hydrostatic actuator for flight control. *Int. J. Fluid Power* **2016**, *17*, 125–145. [CrossRef]
6. Shi, C.; Wang, X.; Wang, S.; Wang, J.; Tomovic, M.M. Adaptive decoupling synchronous control of dissimilar redundant actuation system for large civil aircraft. *Aerosp. Sci. Technol.* **2015**, *47*, 114–124. [CrossRef]
7. Botten, S.L.; Whitley, C.R.; King, A.D. Flight Control Actuation Technology for Next-Generation All-Electric Aircraft. *Technol. Rev. J.* **2000**, *8*, 55–68.
8. Li, D.; Li, Y.; Li, Y.; Zhang, P.; Dong, S.; Yang, L. Study on PMSM Power Consumption of Dual-Variable Electro-Hydraulic Actuator with Displacement-Pressure Regulation Pump. In Proceedings of the 2018 IEEE/ASME International Conference on Advanced Intelligent Mechatronics (AIM), Auckland, New Zealand, 9–12 July 2018; pp. 1172–1177.
9. Hu, W.; Zhou, L.; Tian, Y.; Jiao, Z.; Shang, Y.; Song, Z.; Yan, L. Analysis for the power loss of electro hydrostatic actuator and hydraulic actuator. In Proceedings of the 2015 IEEE International Conference on Advanced Intelligent Mechatronics (AIM), Busan, Korea, 7–11 July 2015; pp. 613–616.
10. Lan, Z.; Wei, X.; Chen, L. Thermal analysis of PMSM based on lumped parameter thermal network method. In Proceedings of the 2016 19th International Conference on Electrical Machines and Systems (ICEMS), Chiba, Japan, 13–16 November 2016; pp. 1–5.

11. Kačenka, A.; Pop, A.; Vintiloiu, I.; Fodorean, D. Lumped Parameter Thermal Modeling of Permanent Magnet Synchronous Motor. In Proceedings of the 2019 Electric Vehicles International Conference (EV), Bucharest, Romania, 3–4 October 2019; pp. 1–6.
12. Chen, Q.; Zou, Z.; Cao, B. Lumped-parameter thermal network model and experimental research of interior pmsm for electric vehicle. *CES Transactions on Electrical Machines and Systems* **2017**, *1*, 367–374. [CrossRef]
13. Mukundan, S.; Dhulipati, H.; Tjong, J.; Kar, N.C. Parameter Determination of PMSM Using Coupled Electromagnetic and Thermal Model Incorporating Current Harmonics. *IEEE Trans. Magn.* **2018**, *54*, 1–5. [CrossRef]
14. Zhang, B.; Qu, R.; Wang, J.; Li, J.; Xu, W.; Chen, Y. Electromagnetic–Thermal Coupling Analysis of Permanent Magnet Synchronous Machines for Electric Vehicle Applications Based on Improved (μ+1) Evolution Strategy. *IEEE Trans. Magn.* **2015**, *51*, 1–10. [PubMed]
15. Wan, Y.; Li, Q.; Guo, J.; Cui, S. Thermal analysis of a Gramme-ring-winding high-speed permanent-magnet motor for pulsed alternator using CFD. *IET Electric Power Applications* **2020**, *14*, 2202–2211. [CrossRef]
16. Jungreuthmayer, C.; Bauml, T.; Winter, O.; Ganchev, M.; Kapeller, H.; Haumer, A.; Kral, C. A Detailed Heat and Fluid Flow Analysis of an Internal Permanent Magnet Synchronous Machine by Means of Computational Fluid Dynamics. *IEEE Trans. Ind. Electron.* **2012**, *59*, 4568–4578. [CrossRef]
17. Wu, S.; Yang, H.; Han, D.; Chang, H.; Huang, X.; Meng, Q. Thermal analysis for hydraulic powering system of a certain type aircraft. In Proceedings of the CSAA/IET International Conference on Aircraft Utility Systems (AUS 2018), Guiyang, China, 19–22 June 2018; 2018; pp. 1–4.
18. Shi, G.; Wang, H. Thermal-hydraulic Model for Axial Piston Pump with Leakage and Friction and Its Application. *Industrial Lubrication and Tribology* **2019**, *71*, 810–818. [CrossRef]
19. Li, C.; Jiao, Z. Calculation Method for Thermal-Hydraulic System Simulation. *J. Heat Transf.* **2008**, *130*, 318–323.
20. Li, K.; Lv, Z.; Lu, K.; Yu, P. Thermal-hydraulic modeling and simulation of piston pump in electro-hydrostatic actuator system. In Proceedings of the 2015 International Conference on Fluid Power and Mechatronics (FPM), Harbin, China, 5–7 August 2015; pp. 1097–1101.
21. Li, K.; Zhong, L.; Kun, L.; Ping, Y. Thermal-hydraulic Modeling and Simulation of the Hydraulic System based on the Electro-hydrostatic Actuator. *Procedia Eng.* **2014**, *80*, 272–281. [CrossRef]
22. Stadlbauer, K.; Poltschak, F.; Rafetseder, D.; Amrhein, W. A SPICE-based lumped parameter thermal model with geometrically distributed elements for electro-hydraulic actuators. In Proceedings of the International Symposium on Power Electronics Power Electronics, Electrical Drives, Automation and Motion, Sorrento, Italy, 20–22 June 2012; pp. 511–516.
23. Ding, X.; Liu, G.; Du, M.; Guo, H.; Duan, C.; Qian, H. Efficiency Improvement of Overall PMSM-Inverter System Based on Artificial Bee Colony Algorithm Under Full Power Range. *IEEE Trans. Magn.* **2016**, *52*, 1–4. [CrossRef]
24. Song, Z.N.; Jiao, Z.X.; Shang, Y.X.; Wu, S.; Hu, W.N. Design and analysis of a direct load sensing electro-hydrostatic actuator. In Proceedings of the 2015 International Conference on Fluid Power and Mechatronics (FPM), Harbin, China, 5–7 August 2015; pp. 624–627.
25. Wang, Y.; Kou, G.; Hu, S. Thermal modeling and analysis of oil-cooled high speed permanent magnet motor in the EHA system. In Proceedings of the CSAA/IET International Conference on Aircraft Utility Systems (AUS 2018), Guiyang, China, 19–22 June 2018; pp. 710–715.
26. Rehman, Z.; Seong, K. Three-D Numerical Thermal Analysis of Electric Motor with Cooling Jacket. *Energies* **2018**, *11*, 92. [CrossRef]
27. Park, J.; Moosavi, M.; Toliyat, H.A. Electromagnetic-thermal coupled analysis method for interior PMSM. In Proceedings of the 2015 IEEE International Electric Machines & Drives Conference (IEMDC), Coeur d'Alene, ID, USA, 10–13 May 2015; pp. 1209–1214.
28. Zhang, J.; Li, Y.; Xu, B.; Chen, X.; Pan, M. Churning losses analysis on the thermal-hydraulic model of a high-speed electro-hydrostatic actuator pump. *Int. J. Heat Mass Transf.* **2018**, *127*, 1023–1030. [CrossRef]
29. Hong, G.; Wei, T.; Ding, X.; Duan, C. Multi-Objective Optimal Design of Electro-Hydrostatic Actuator Driving Motors for Low Temperature Rise and High Power Weight Ratio. *Energies* **2018**, *11*, 1173. [CrossRef]